

Characterization of Nickel Diffusion and its Effect on the Microstructure of Nickel PM Steels

BERNARD TOUGAS, CARL BLAIS, FRANÇOIS CHAGNON,
and SYLVAIN PELLETIER

Admixing pure elements to powder mixes can cause the formation of heterogeneous microstructures in sintered parts. For instance, nickel is renowned for forming nickel-rich areas (NRA) in powder metallurgy (PM) nickel steels due to its poor diffusivity in iron matrix (or lattice). The present work is aimed at characterizing the principal diffusion mechanisms of nickel and their influence on microstructures and properties of PM nickel steels. A new wavelength dispersive X-ray spectrometry (WDS) approach linking line scans and X-ray maps to concentration maps is proposed. Grain boundary and volume diffusion coefficients of admixed nickel have been determined in PM nickel steels using Suzuoka's equation. Results also show that nickel distributes itself in the iron matrix mainly by surface and grain boundary diffusion.

DOI: 10.1007/s11661-012-1417-9

© The Minerals, Metals & Materials Society and ASM International 2012

I. INTRODUCTION

ONE of the many advantages that the powder metallurgy (PM) process offers is its flexibility toward final chemical composition. In the case of PM steels, alloying elements can be admixed, prealloyed (or both) to the base powder to yield a rather wide variety of microstructures upon sintering.^[1]

Admixing pure elements to powder mixes can cause the formation of heterogeneous microstructures in sintered parts. This is mostly the case when substitution solid solution elements are admixed. It is well known that substitution elements have lower diffusion rates than interstitial elements.^[2] Moreover, diffusion coefficients of an element vary with alloy chemistry. Lower diffusion rates, at a given sintering temperature, can lead to significant heterogeneity in the microstructure of PM parts.^[3]

Nickel is one of the most popular admixed elements in PM steels and is one of the chemical elements that increases the most the strength of PM steels as highlighted (FN-) in Figure 1.

Nevertheless, admixed nickel is well known to produce nickel-rich areas (NRA) that are usually found near the original locations of nickel particles that did not disperse (or diffuse) uniformly in the steel matrix during sintering.^[5] Typically, between 1 and 4 wt pct of

nickel is added to PM steel powder mixes to increase hardenability and consequently mechanical properties.^[4] However, the presence of NRA, which contain much more nickel than the targeted alloy chemistry, generally leads to the formation of retained austenite.

As it was recently pointed out,^[5] the literature on the use of nickel in PM steels is somewhat confusing with regards to admixed nickel distribution in the iron matrix during sintering. This observation highlights the fact that the mechanisms of nickel diffusion in PM steels are still misunderstood by many researchers. The present work is aimed at characterizing the principal diffusion mechanisms of nickel and their influence on PM steel microstructures and properties.

II. VOLUME DIFFUSION

Uniformly distributed admixed nickel is rarely obtained in iron-nickel (FN) steel series for conventional sintering conditions [1394 K (1121°C)—30 minutes]. Nickel heterogeneity comes from its low volume (lattice) diffusion coefficient in austenite (Fe_γ). Several papers report nickel volume diffusion coefficients in austenite, but deviations between values are significant.^[7–11] Million *et al.*^[6] explained this difference by the randomness of grain boundaries and the variability of lattice defects between specimens characterized. However, they all showed that nickel diffuses in iron at a fraction of the self-diffusion coefficient of iron at austenitizing temperatures. Figure 2 shows the volume diffusion ratio between nickel and iron diffusing in Fe.^[6,7] These results show that for a typical sintering temperature of 1394 K (1121°C), the nickel diffusion rate in iron only represents 40 pct of iron self-diffusion rate.

As stated above, the presence of nickel-rich areas (NRA) in PM nickel steel is due to the incomplete distribution of nickel. On the other hand, nickel diffusion

BERNARD TOUGAS, Project Leader, is with the Department of Mining, Metallurgical and Materials Engineering, Université Laval, 1065 De la Médecine, Québec, QC, G1V 0A6, Canada, and also with Centre de Métallurgie du Québec (CMQ); 3095 Westinghouse, Trois-Rivières, QC, Canada. Contact email: bernard.tougas@cegepr.qc.ca
CARL BLAIS, Professor, is with the Department of Mining, Metallurgical and Materials Engineering, Université Laval. FRANÇOIS CHAGNON, Principal Scientist, is with Rio Tinto Metal Powders, 1655 rte Marie-Victorin, Sorel-Tracy, QC, J3R 4R4, Canada. SYLVAIN PELLETIER, General Manager Automotive Portfolio, is with National Research Council of Canada, 75 boul. de Mortagne, Boucherville, QC, J4B 6Y4, Canada.

Manuscript submitted December 9, 2011.

Article published online September 27, 2012

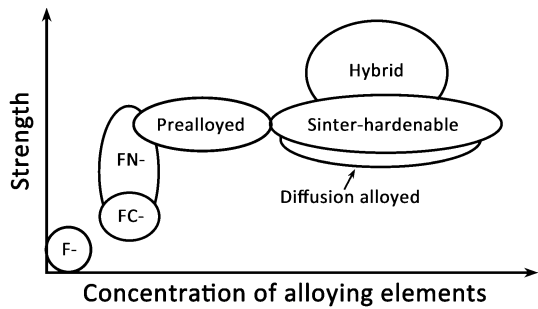


Fig. 1—Schematic representation of the variation of strength as a function of concentration of alloying elements for the main series of PM steels referenced in Metal Powder Industries Federation Standard 35.^[4]

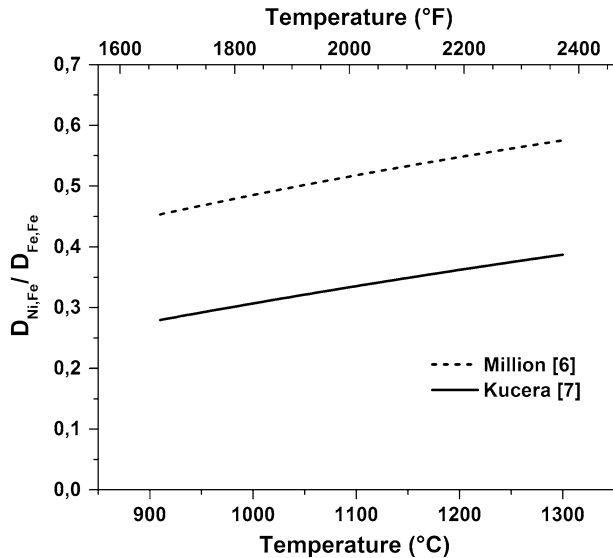


Fig. 2—Ratio of volume diffusion coefficient between nickel and iron diffusing into Fe_γ. Adapted from data presented in Refs. [6,7].

in the steel matrix is not the only mechanism that can lower the volume fraction of NRA during sintering. Indeed, other elements will diffuse in the volume occupied by original nickel particles, thus decreasing the local nickel concentration. In fact, Figure 3 clearly shows that the diffusion coefficient of iron in nickel ($D_{Fe,Ni}$) is higher than the opposite ($D_{Ni,Fe}$).^[6] Already, Figures 2 and 3 indicate that nickel diffuses more slowly than iron in both pure metals (iron and nickel). Therefore, we can expect that nickel will diffuse partially into iron and that it is mostly iron diffusing into nickel particles that will lower the local nickel concentration.

The diffusion coefficients presented above are for volume diffusion. It is well known that this mechanism is mainly observed in the intermediate and final stages of sintering because it has a higher activation energy compared to surface diffusion.^[12] Moreover, conventional sintering [*i.e.* 1394 K (1121°C) for 30 minutes] only reaches the beginning of the intermediate stage.^[11] In addition, the local chemistry is constantly changing during sintering. Million *et al.*^[6] report that diffusion is highly affected by the presence of solid solution elements

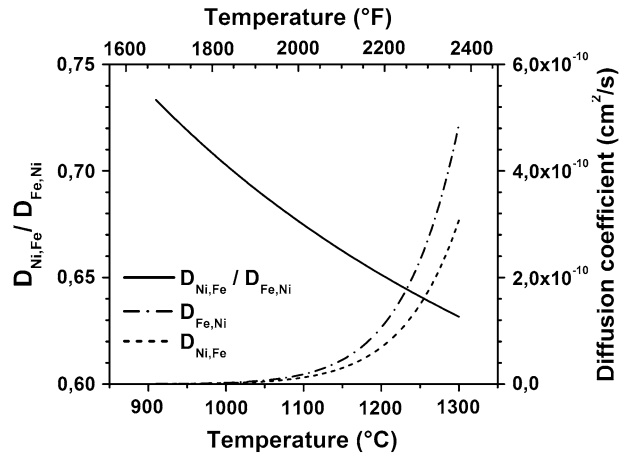


Fig. 3—Diffusion coefficient and ratio between nickel diffusing in iron ($D_{Ni,Fe}$) and iron diffusing in nickel ($D_{Fe,Ni}$). Adapted from data presented in Ref. [6].

and/or by the formation of phases with the diffusing atoms. Figures 4 and 5 show a summary of the diffusion coefficients of iron and nickel in a Fe-Ni binary alloy as a function of chemistry and temperature. It is seen that for most of the temperature and concentration combinations, volume diffusion of iron (Fe) is greater than that of nickel (Ni). Nevertheless, this behavior is reversed when the concentration of nickel falls between 40 and 85 at. pct. The authors of the papers from which the data were extracted noted that this change in behavior happened in a range of concentrations close to where FeNi₃ is stable at lower temperatures. However, they did not propose any explanation for the cause of this reversal.

III. GRAIN BOUNDARY DIFFUSION

A grain boundary can be defined as the interfacial transition region between two grains in contact but with different crystallographic orientations.^[3] It can also represent the interface between two different phases. In addition, grain boundary diffusion (D_{GB}) represents atomic transport due to the random displacement of atoms along grain boundaries. The mechanism of grain boundary diffusion (D_{GB}) is known to have the smallest activation energy within the bulk transport mechanisms.^[12,13] Therefore, it is usually the first bulk transport mechanism observed during sintering. D_{GB} is affected by several parameters such as: grain boundary thickness, disorientation, the proportion of solute atoms and the saturation level of the grain boundary.^[3,14] The purer, the thicker and the more heavily disoriented a grain boundary is: the lower is the diffusion activation energy. Nevertheless, D_{GB} is hard to characterize at high temperature because the diffusing atoms are dragged out of grain boundaries by volume diffusion which is more active at high temperature. Consequently, only a few articles have characterized nickel grain boundary diffusion coefficient in iron.^[14–17] Divinski *et al.*^[14] have characterized the nickel volume and grain boundary diffusion for a 40 to 60 wt pct Ni-Fe binary alloy.

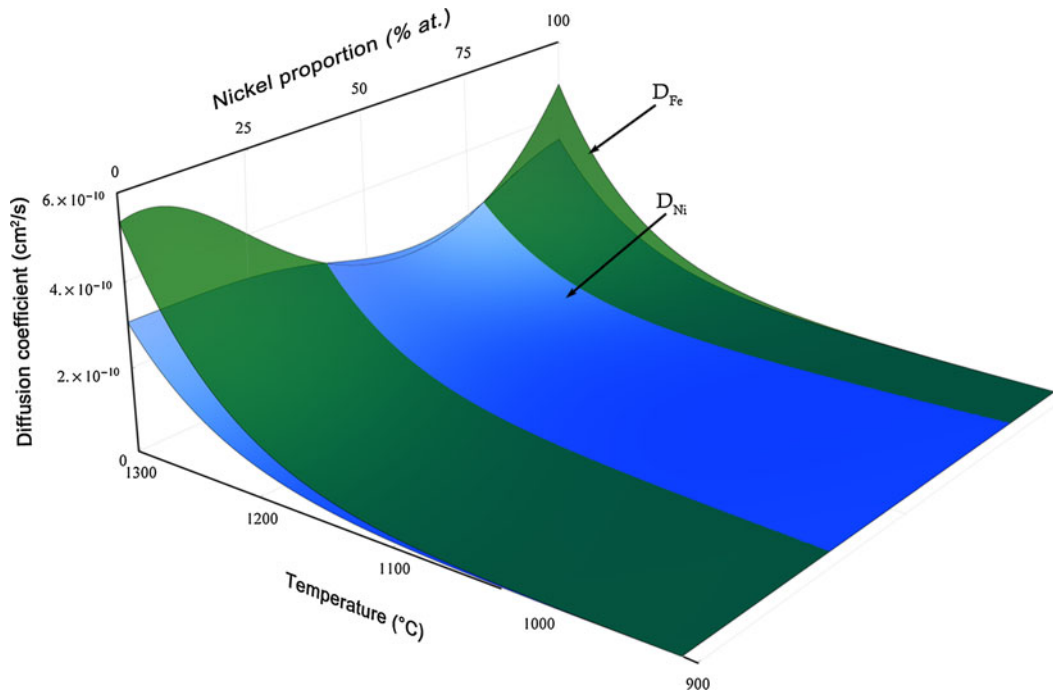


Fig. 4—Volume diffusion coefficients of iron (D_{Fe}) and nickel (D_{Ni}) in Fe-Ni system. Adapted from data presented in Ref. [6].

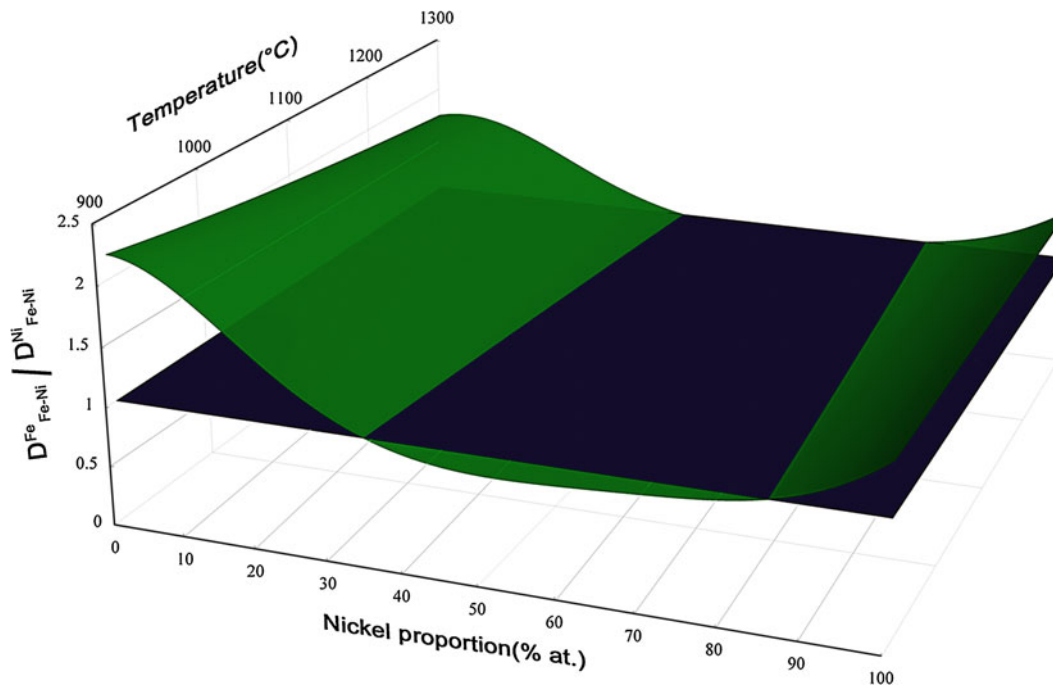


Fig. 5—Volume diffusion coefficient ratio $D_{Fe-Ni}^{Fe} / D_{Fe-Ni}^{Ni}$ for the Fe-Ni system. Adapted from data presented in Ref. [6].

Figure 6 presents the ratio of D_{GB} / D_V adapted from the data presented in Reference 14. If we assume that the relationship still holds at higher temperatures, we can estimate by extrapolation that D_{GB} is roughly 30 000 times greater than D_V at 1173 K (900 $^{\circ}\text{C}$) and 1000 time greater at 1323 K (1050 $^{\circ}\text{C}$).

PM sintering is a complex process that involves several diffusion mechanisms that operate at the same time. Therefore the present work is aimed at characterizing the principal diffusion mechanisms that use admixed nickel in a conventional sintering process for components made from PM nickel steels.

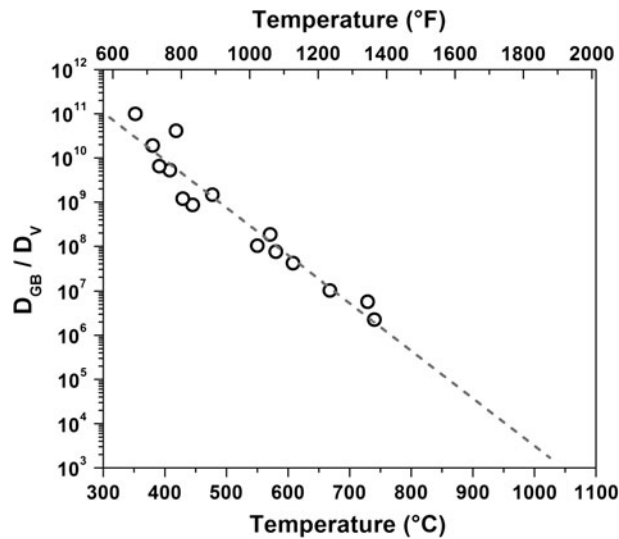


Fig. 6—Nickel D_{GB}/D_V ratio for an 40 to 60 wt pct Ni-Fe alloy. Adapted from data presented in Ref. [14].

IV. METHODOLOGY

A. Specimens Preparation

Characterization of admixed nickel diffusion in PM nickel steels was carried out on transverse rupture strength bars (TRS) sintered at different temperatures. The base powder used for the project was the ATOMET 4901 ($D_{50} = 83 \mu\text{m}$) from Rio Tinto Metal Powders. Table I presents the powder chemistry of ATOMET 4901, which is prealloyed with manganese (Mn) and molybdenum (Mo). A premix was prepared using 0.65 wt pct of graphite (TIMREX Synthetic graphite grade KS6) and 2.00 wt pct of nickel [Inco 123 ($D_{50} = 8 \mu\text{m}$)]. The targeted final chemistry is presented in Table II. Die walls lubrication with zinc stearate was used to minimize all possible interactions between lubricant and the diffusing elements. TRS bars were pressed to a green density of 7.1 g/cm^3 and sintered at 1223 K, 1323 K and 1423 K (950 °C, 1050 °C, and 1150 °C) for 30 minutes in an 90 to 10 vol. pct $\text{N}_2\text{-H}_2$ atmosphere with a cooling rate of 0.75 K/s between 1223 K and 723 K (900°C and 450°C). A total of five specimens per condition were used.

B. Specimens Characterization

Chemistry, dimensional change from green size, porosity measurement and transverse rupture strength were characterized for each sintered sample according to the ASTM standard E-1019 and MPIF standards, 44, 57 and 41 respectively.

X-ray maps and line scans of the main alloying elements (Fe, Mn, Mo, Ni) were acquired using wavelength dispersive X-ray spectrometry (WDS) with a CAMECA SX-100 microprobe. These two types of analyses were carried out in areas where NRA could be identified in backscattered electron imaging (BSE). Mapping intensity scale was kept

Table I. Base Powder Chemistry: ATOMET 4901

Elements	Fe	C	Mo	Mn	S	O
Proportion (wt pct)	bal.	0.004	1.48	0.13	0.0086	0.08

Table II. Targeted Sintered Chemistry

Elements	Fe	C	Ni	Mo	Mn
Proportion (wt pct)	bal.	0.60	2.00	1.45	0.10

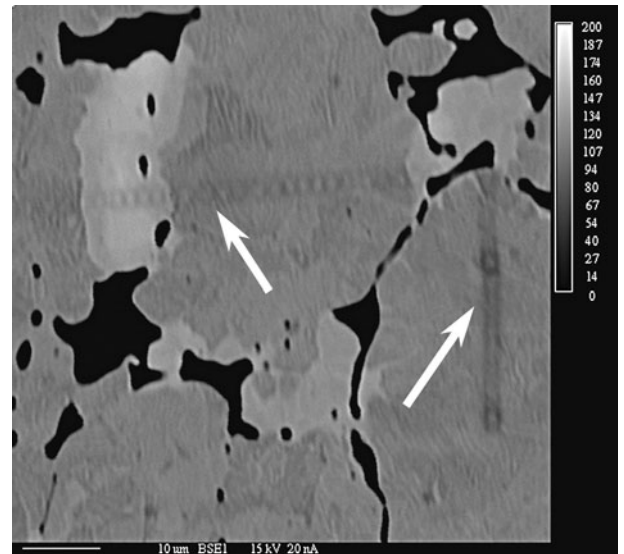


Fig. 7—BSE micrograph showing distinctive circular traces leaved by line scans microprobe analysis.

constant for each element so that all specimens can be easily compared even though this approach may have caused signal saturation in certain areas.

Note that care was taken to select the optimum magnification to minimize overlap of the X-ray generation volume from one location to the next during X-ray mapping and line scan acquisition. Thus, Monte-Carlo simulations were performed to determine the ideal magnification as a function of the chemistry of the alloy.

1. Nickel Mappings to Quantitative Results

In order to minimize acquisition time, an entire area of interest was not quantitatively analyzed with WDS. Instead, line scan results were correlated to acquired maps. As presented in Figure 7, line scan analysis leaves distinctive circular traces on the specimen at each location where an analysis was performed. These patterns were used to carry out a linear regression between the concentrations measured with the line scans and the gray-scale X-ray maps. More precisely, each pixel making out the map was converted into a specific RGB (red blue green) value to build a matrix. Note that for grayscale images, RGB value can be represented by

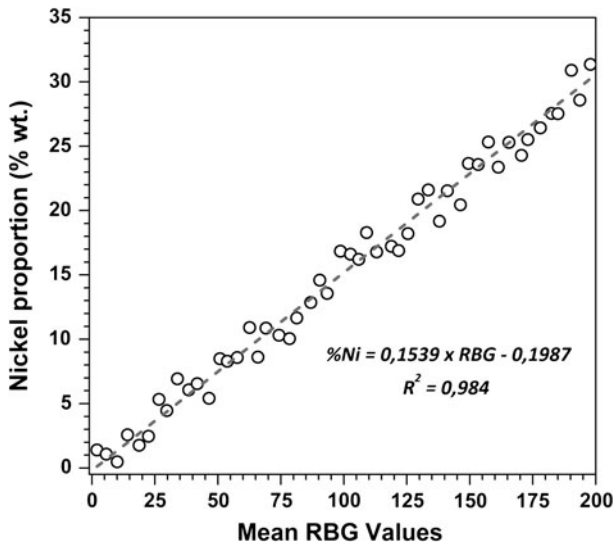


Fig. 8—Linear relationship between WDS maps RGB values and line scan nickel proportions.

only one number for each shade of gray. Then, RGB averages (from 0 to 255) within each circle were then extracted and fitted against line scan results. This relationship was used to convert all RGB matrices into nickel weight percent matrices as presented in Figure 8. Following this transformation, three dimensional (3D) plots of the weight percent of nickel were built for each area of interest. Finally, optical micrographs of each area of interest were superimposed on the corresponding plots to characterize the phases in the final microstructure as a function of nickel concentration. Delimitation of each phase was done using image analysis performed in optical micrographs etched in 2 pct nital. The image analysis system used was a Clemex Vision PE 5.0 equipped with an Olympus GX51 microscope. Figure 9 summarizes schematically the conversion steps.

A total of nine X-ray maps representing each a surface of $6400 \mu\text{m}^2$ were analyzed by this technique. An example showing the main steps of the technique is presented in Figure 10 where optical micrograph (A), mapping (B) and calculated nickel proportion (C and D) are presented respectively.

C. Volume and Grains Boundary Diffusion Coefficient Determination

Several analytical models have been developed in the existing literature to characterize volume and grain boundary diffusion coefficients.^[18–20] Among the most cited, Suzuoka's instantaneous source model seems the more appropriate for this case since it considers a finite number of diffusing atoms in the system. It consists of a finite source, perpendicular to a grain boundary in a polycrystal containing cubic grains as described in Figure 11. This model differentiates the contributions of volume (c_1) and the grain boundary diffusion (c_2).

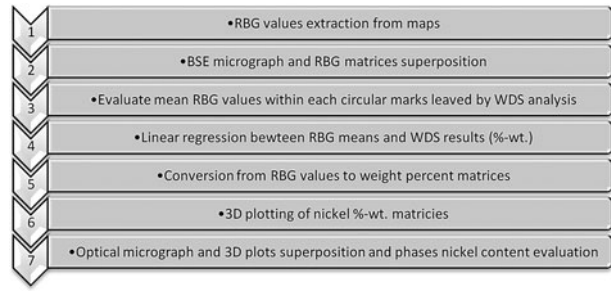


Fig. 9—Conversion steps used to characterize the spatial distribution of nickel.

Equation [1] details Suzuoka's model as a Laplace transform.

$$C(y, t) = \frac{K}{\sqrt{\pi D_V t}} \left(c_1 + c_2 \frac{2\sqrt{D_V t}}{L} \right) \quad [1]$$

$$c_1 = e^{(-\eta^2/4)}$$

$$c_2 = \int_1^\Delta \frac{1}{s^{3/2}} \cdot \frac{\eta^2}{s-2} \cdot e^{(-\eta^2/4s)} \cdot \sqrt{\frac{\Delta-1}{\Delta-s}} \cdot \left[\frac{e^{(-X^2)}}{s-2} - X \cdot \text{erfc}(X) \right] ds$$

With following dimensionless variables:

$$X = \sqrt{\frac{\Delta-1}{\Delta-s}} \cdot \frac{s-1}{\beta} \quad \eta = \frac{y}{\sqrt{D_V t}}$$

$$\beta = \frac{2a(\Delta-1)}{\sqrt{D_V t}} \quad \Delta = \frac{D_{GB}}{D_V}$$

K represents the amount per unit of area of solute at the source, y represents the distance from the surface (cm), $2a$ is the grain boundary width 2.5×10^{-8} cm, t the time (s), L half of the grain edge length (cm) [mean grain size diameter was used ($2L$)], D_V the volume diffusion coefficient (cm^2/s) and D_{GB} the grain boundary diffusion coefficient (cm^2/s).

Converted maps of the distribution of the wt pct of nickel (Figure 10(c)) were used to extract the appropriate data to characterize the diffusion coefficients of nickel. The idea was to identify an area where an originally admixed nickel particle is located perpendicular to one grain boundary. Thus, from the converted concentrations map, the local concentrations of nickel in the vicinity of grain boundaries and in the center of the grain can be obtained. Once this data was generated, Suzuoka's model was solved numerically to obtain the volume and grain boundary diffusion coefficients for each sintering temperature studied. Romberg quadrature numerical integration method with least squares iterations was used to solve the equation.^[21]

In this study, the variation of pore size, shape and volume fraction was not considered in the evaluation of the diffusion coefficients since the approach followed considered only a single nickel particles and an intersecting

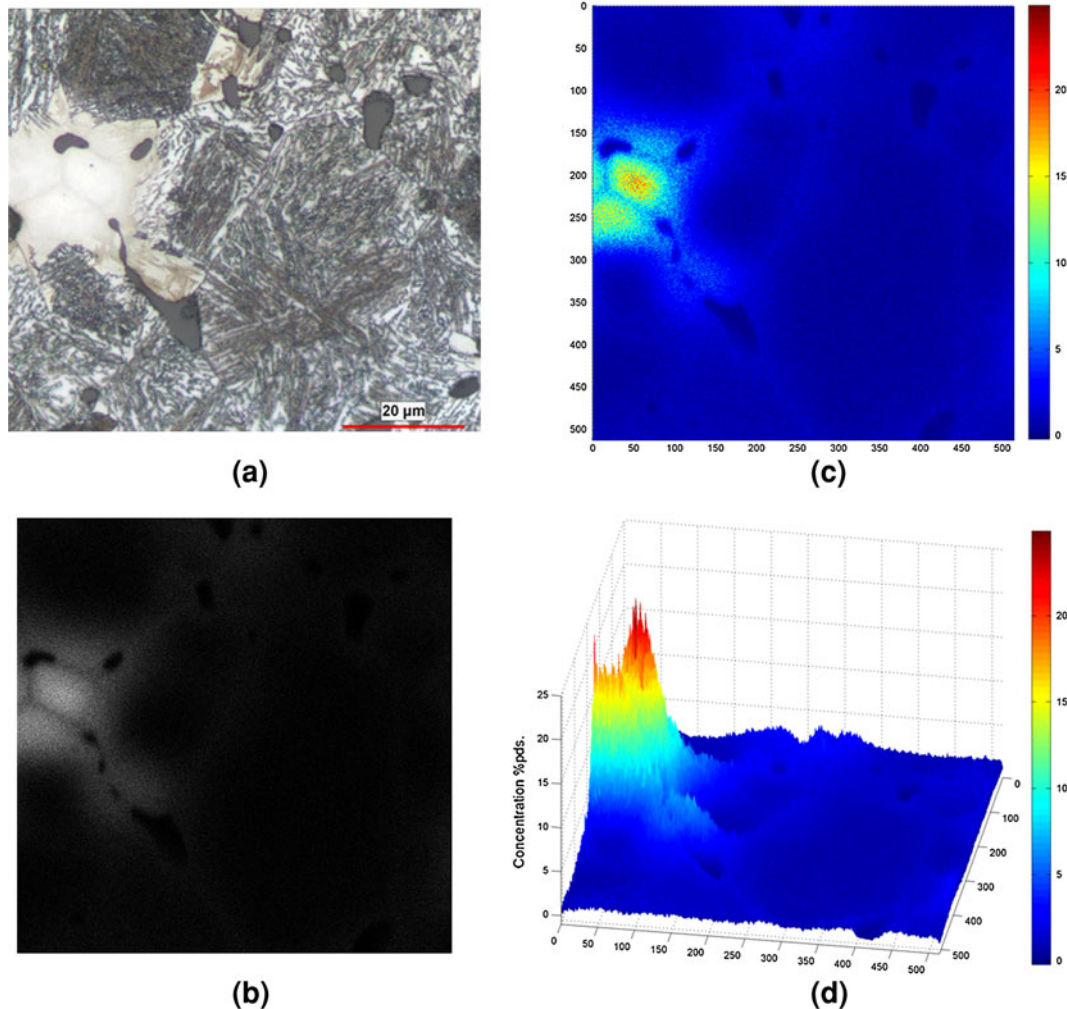


Fig. 10—Example given by the maps to proportion conversion. (a) Optical micrograph of the region of interest; (b) X-ray mapping of Ni in gray scale (c) and (d) presents the calculated Ni wt pct.

grain boundary for each analysis. Thus, the effects related to porosity were considered negligible. This is also the reason why surface diffusion was not considered in this study. Nevertheless, if this technique and the results it generated were to be used at a more macroscopic scale, it would have to include these factors as they would most likely influence several diffusion mechanisms, surface diffusion being the most sensitive.

V. RESULTS AND DISCUSSION

A. Standard PM Characterization

The average chemical analyses show that sintered parts have comparable compositions (Table III).

As expected, characterization of the dimensional change, the porosity level and the transverse rupture strength shows that higher sintering temperatures enhance densification as well as mechanical properties (Figure 12; Table IV).

The swelling observed for sintering temperatures of 1223 K and 1323 K (950 °C and 1050 °C) is linked to

the diffusion of admixed graphite. In the present case, graphite and nickel were added in their native form to the powder blend. Upon heating, graphite diffuses completely into the iron matrix creating the observed expansion while nickel diffusion is much less important. As stated above, it is mainly iron that diffuses into nickel. Thus, three competing phenomena take place. Graphite and, to a lesser extent, nickel diffusion in iron brings swelling of the specimen while iron diffusing into nickel as well as self-diffusion cause shrinkage. As the sintering temperature increases, densification induced by iron self-diffusion and diffusion into nickel become more important to a point where it overcomes the swelling due to carbon diffusing in austenite and dilating the iron matrix. This can also be observed with dilatometry tests that have been performed on green compacts.

Figure 13 shows that admixed diffusion expansion predominantly occurring after the ferrite to austenite transformation ($\alpha \rightarrow \gamma$) upon heating. In parallel, bulk diffusion mechanisms produce densification. Part of this densification can be observed on curves at holding temperature. Note that different dimensional change

results can be seen between the dilatometry testing and the TRS dimensional change. Divergence source is unknown, but it is possible that geometry and/or temperature profile differences between the two experiments were in cause. Interestingly, the three curves

show that densification (or α sintering^[22]) is taking place before the austenite transformation. Since surface diffusion mechanisms do not cause densification, only bulk diffusion mechanisms can have caused the decrease in thermal expansion between 973 K and 1073 K (700 °C and 800 °C).^[12] Moreover, as seen in Sect. III, grain boundary diffusion is several order of magnitude greater than volume diffusion in this range of temperatures. Therefore, we can conclude that it was this mechanism that caused the deflection.

It is important to note that, in this study, nickel is not the only element diffusing in iron during sintering and that carbon (admixed graphite) diffuses as well. Nevertheless, carbon diffuses following an interstitial diffusion mechanism that is prevalent at lower temperature (see arrow in Figure 13) than for nickel (which follows a vacancy diffusion mechanism). Thus, it is important to note that the diffusion coefficients measured in Sect. V-D should only be relevant for nickel PM steels of similar chemical composition.

B. Characterization of Nickel Diffusion

Figures 14, 15 and 16 present typical results of the consequence of nickel diffusion as a function of the sintering temperature studied. Iron and nickel mapping, line scan, microstructures and BSE micrograph are presented.

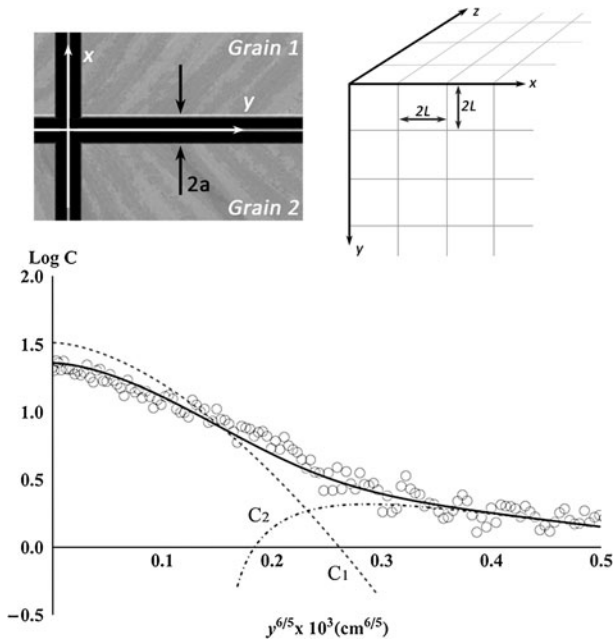


Fig. 11—Presentation of Suzuoka's model.^[20]

Table III. Sintered Bars Average Chemical Analysis

Temperature [K (°C)]	Proportion (wt pct)				
	Fe	C	Ni	Mo	Mn
1223 (950)	bal.	0.600	2.02	1.42	0.17
1323 (1050)	bal.	0.594	1.99	1.43	0.17
1423 (1150)	bal.	0.623	1.95	1.45	0.16

Table IV. Porosity Level for Each Sintering Temperature

Temperature [K (°C)]	Porosity Level (Pct)	Δ Green Compact
Green compact	8.92	–
1223 (950)	9.28	0.36
1323 (1050)	9.01	0.09
1423 (1150)	8.68	–0.24

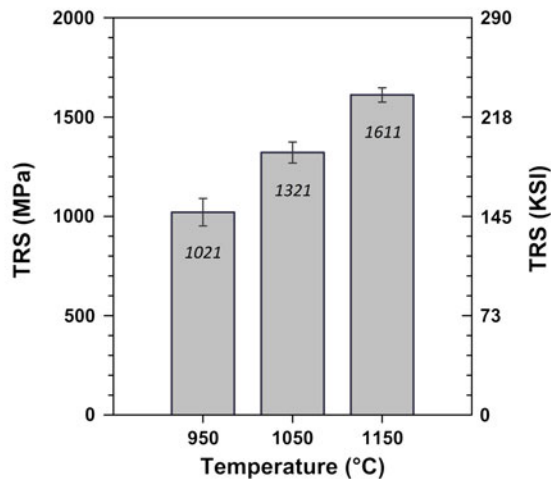
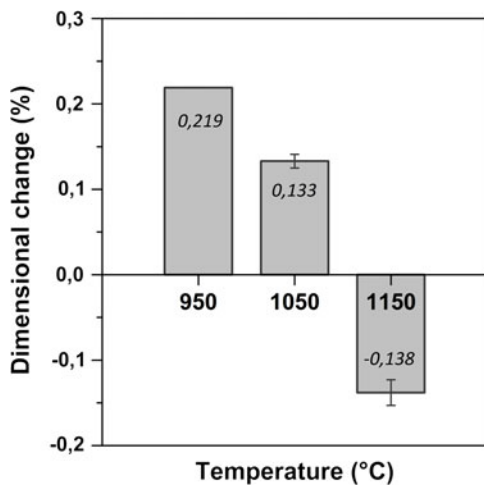


Fig. 12—Average variation of dimensional change of TRS bars from green size and transverse rupture strength as a function of sintering temperatures.

1. Diffusion Mechanisms

At lower sintering temperature [1223 K (950 °C)], it can be seen that surface diffusion (D_S) and grain boundary diffusion (D_{GB}) mechanisms are initiated before volume diffusion. Figure 14(c) shows that particles' surfaces are rich in nickel and that grain boundaries connected to these surfaces are also rich in nickel while the latter is absent in the central area of each grain. At 1323 K (1050 °C), grain boundary diffusion has progressed as shown in Figure 15. Volume diffusion has

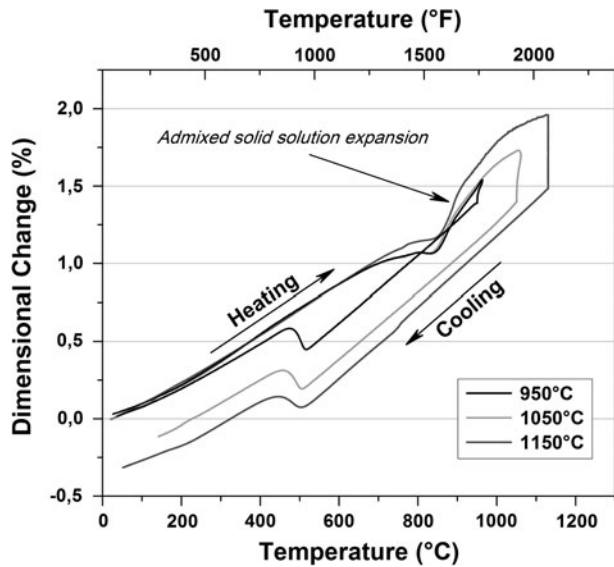


Fig. 13—Dilatometry curves at the three sintering temperature [1223 K, 1323 K, and 1423 K (950 °C, 1050 °C, and 1150 °C)].

started, but nickel is still highly concentrated in the vicinity of grain boundaries. As it was the case for the specimens sintered at 1223 K (950 °C), the microstructure is mainly composed of pearlite and nickel-rich areas (NRA).

At 1423 K (1150 °C), martensite can be observed at several locations in the optical micrograph. Moreover, nickel concentration is significantly more dispersed. Volume diffusion has carried nickel deeper into the particles but still does not reach the central region of larger particles.

Figure 17 compares nickel diffusion distance towards the center of iron particles of similar size as a function of sintering temperature. It shows that, even at 1423 K (1150 °C) for 30 minutes, nickel volume diffusion is limited. The maximum diffusion distance reached by nickel toward the center of the iron particles was only of 5, 10 and 20 μm for sintering temperatures of 1223 K, 1323 K, and 1423 K (950 °C, 1050 °C, and 1150 °C) respectively. Therefore, it is conservative to state that the use of a base powder with a $D_{50} > 40 \mu\text{m}$ will never reach a uniform nickel dispersion and therefore a uniform microstructure using the sintering conditions studied.

Line scans results confirm that iron diffuses much more rapidly into nickel than vice versa. As an example, after sintering at 1423 K (1150 °C), iron constitutes 80 pct of the chemistry of the area where the original nickel particles were located in Figure 16. A second important observation is that manganese and molybdenum prealloyed in the base powder also diffused into the area where the original nickel particles were located. This situation must have influenced the diffusion behavior of nickel as well as the local hardenability. Eventually, these interactions will be studied to refine our analysis of nickel diffusion.

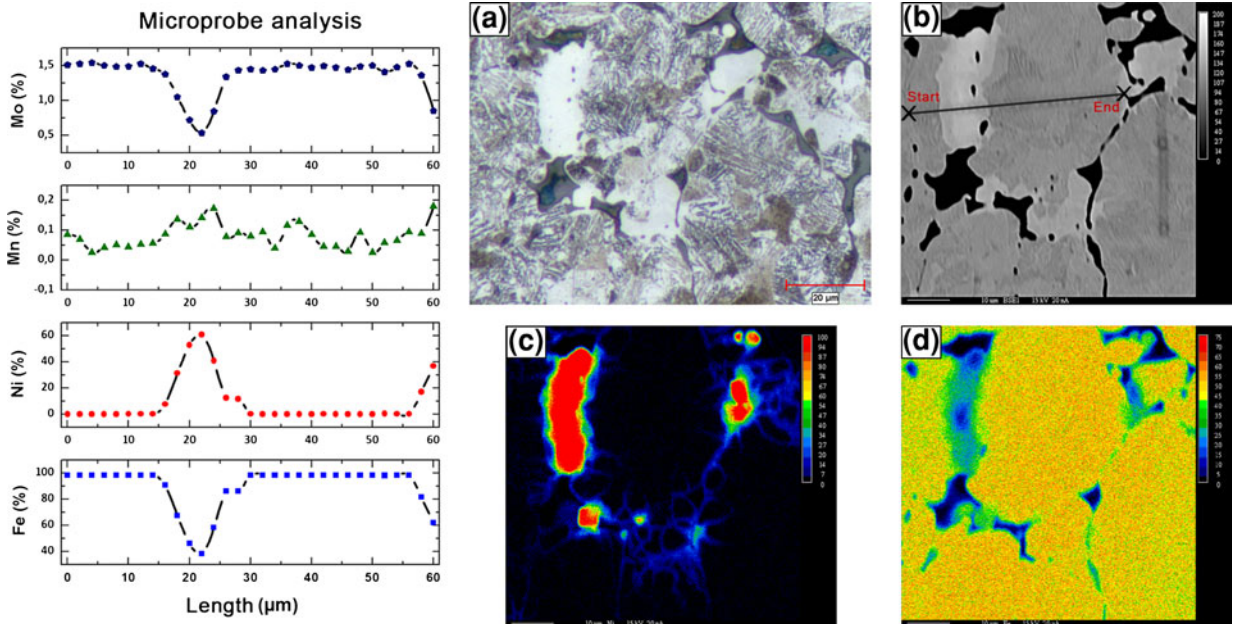


Fig. 14—Typical results for specimen sintered at 1223 K (950 °C). (a) Optical micrograph of the area of interest showing a microstructure of pearlite with NRA, (b) backscatter electron image of the area shown in (a), (c) Microprobe X-ray map of nickel, (d) Microprobe X-ray map of iron.

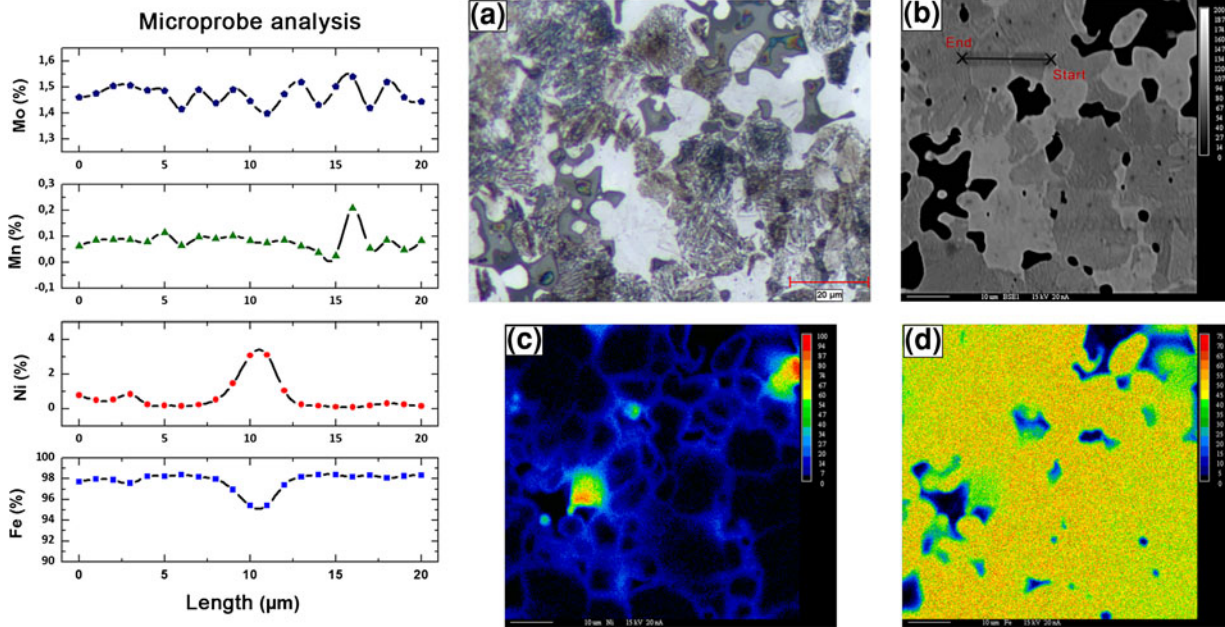


Fig. 15—Typical results for specimen sintered at 1323 K (1050 °C). (a) Optical micrograph of the area of interest showing a microstructure of pearlite with NRA, (b) backscatter electron image of the area shown in (a), (c) Microprobe X-ray map of nickel, (d) Microprobe X-ray map of iron.

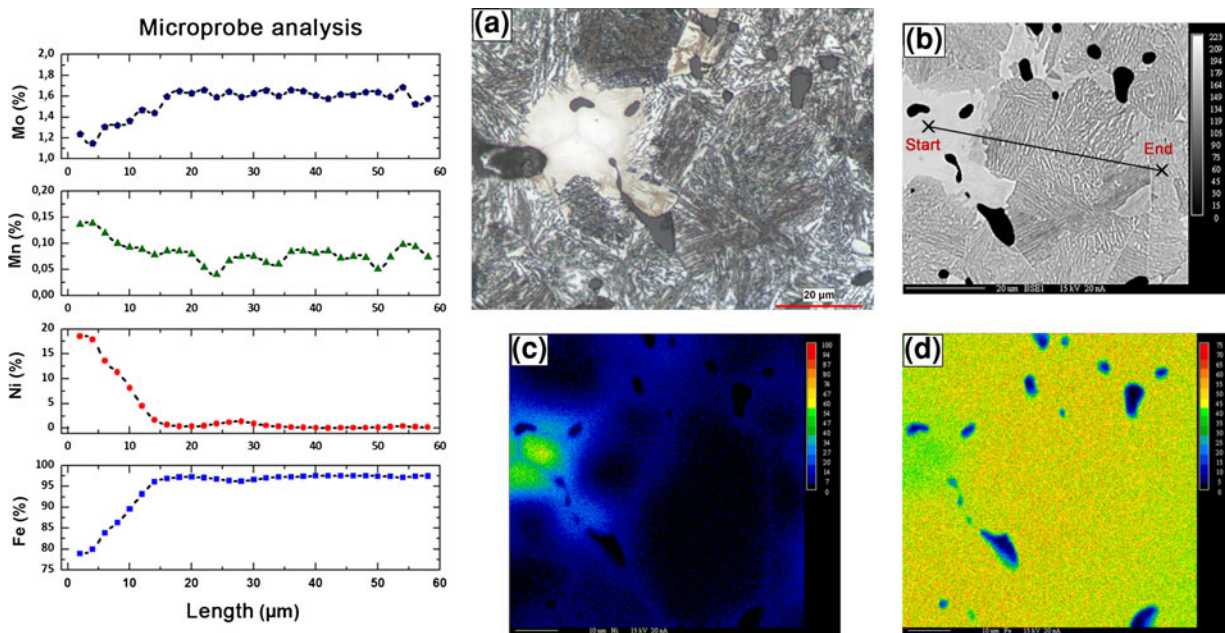


Fig. 16—Typical results for specimen sintered at 1423 K (1150 °C). (a) Optical micrograph of the area of interest showing a microstructure of pearlite with NRA, (b) backscatter electron image of the area shown in (a), (c) Microprobe X-ray map of nickel, (d) Microprobe X-ray map of iron.

C. Phases and Nickel Content Correlation

Correlation between nickel concentrations and microstructure was carried out using line scans and the converted X-ray maps (ref. Figure 10). The areas corresponding to each phases (Bainite-Pearlite, Martensite and Retained Austenite) were compared to the nickel weight

percent converted X-ray maps. Results give the concentration intervals of nickel that promotes the formation of each phase (Figure 18). Table V presents the average concentrations of nickel that favor each phases. Note that the base powder is prealloyed with manganese and molybdenum (Table I).

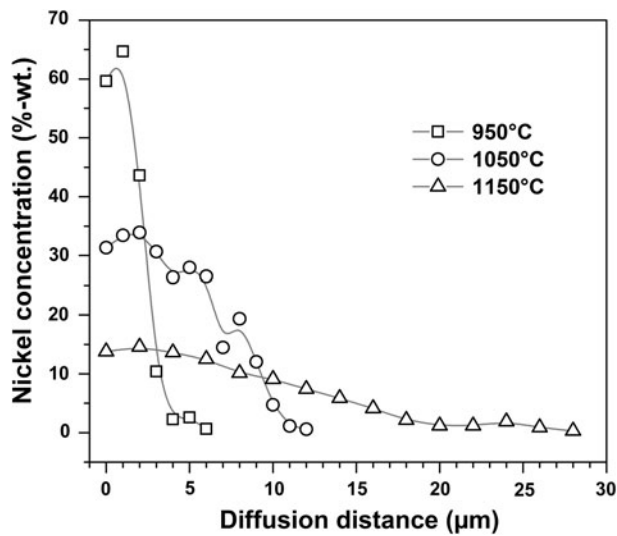


Fig. 17—Nickel diffusion distance toward the center of iron particles for three sintering temperatures.

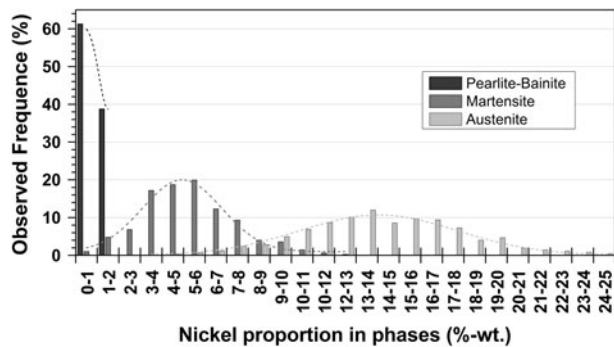


Fig. 18—Nickel concentration normally distributed intervals where each phase is favored.

Table V. Average Nickel Proportions Which Favor Each Phase Formation

	Average (wt pct)	Standard Deviation
Pearlite-Bainite	0.8	0.6
Martensite	5.3	2.1
Retained Austenite	14.3	3.8

D. Nickel Volume and Grain Boundary Diffusion Coefficients in Steel

In addition to enable a correlation between nickel content and microstructure, the converted X-ray maps were used to determine the volume and grain boundary diffusion coefficients of nickel in PM nickel steels. Equation [1] was applied to the data from line scans selected from the different maps acquired. Figure 19 presents the resulting fitted curve for each sintering temperature. As shown, the fitted curves match precisely the extracted data from the converted wt pct maps. Since the exercise was done for three sintering temperatures, it is possible to represent our results using

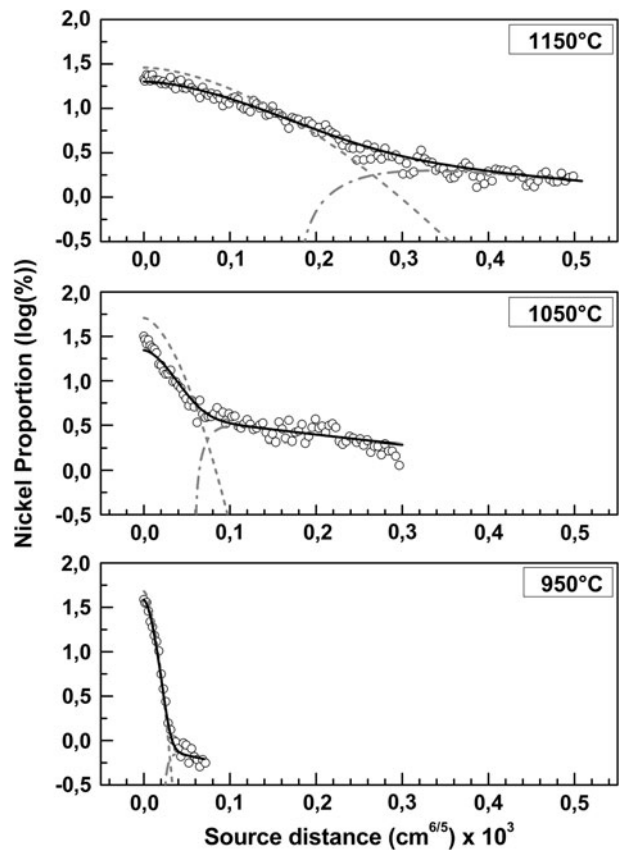


Fig. 19—Suzuoka's model (Eq. [1]) applied to the converted maps for the sintered specimens.

Table VI. Presentation of the Solved Diffusion Coefficients

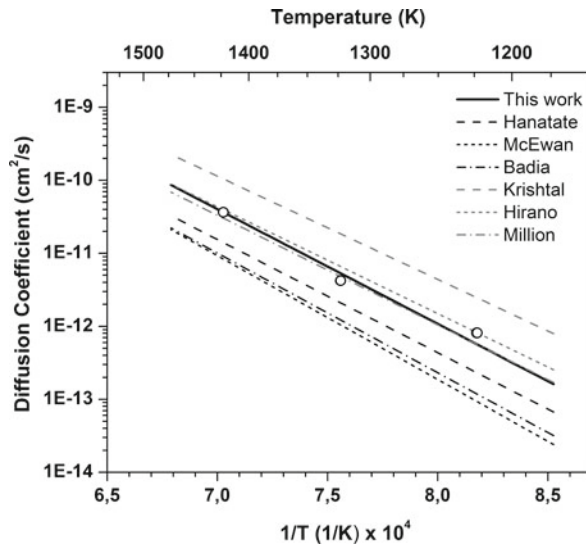
Temperature [K (°C)]	D_V (cm ² /s)	D_{GB} (cm ² /s)
1223 (950)	8.12×10^{-13}	5.37×10^{-7}
1323 (1050)	4.22×10^{-12}	2.75×10^{-6}
1423 (1150)	3.65×10^{-11}	9.14×10^{-6}

Arrhenius' equation. Thus, using the solved diffusions coefficient (D_V and D_{GB}) (Eq. [1]), weighted least square analysis on an Arrhenius model was performed to determine the pre-exponential factor D_0 and the activation energy (Q) for each diffusion coefficient (Eq. [2]). The results are presented in Table VI and compared with published data in Figures 20 and 21. Comparison with results from the literature shows that our findings match precisely what is reported. This observation constitutes one more proof that the technique proposed in this paper can be used to quantitatively characterize diffusion mechanisms in PM materials.

$$D = D_0 \exp(-Q/RT) \quad [2]$$

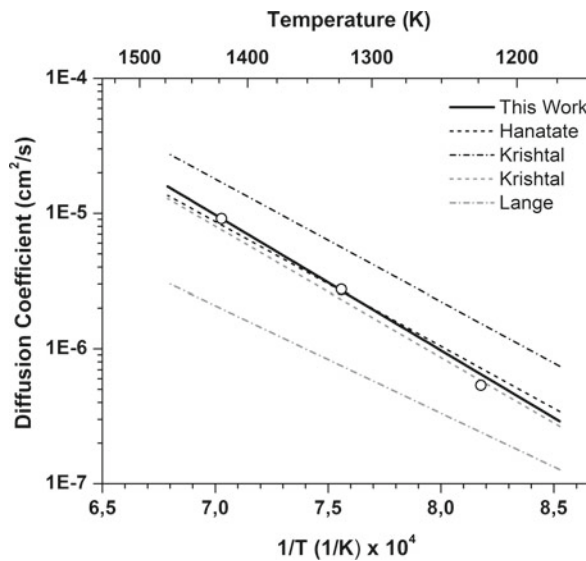
VI. CONCLUSIONS

The goal of this study was the characterization of the main diffusion mechanisms of nickel during the sintering



Paper	D_0 (cm^2/s)	Q (kJ/mol)
This work	4.05	300.9
Hanatate	1.09	296.7
McEwan	6.92	324.7
Badia	3.00	313.8
Krishta	0.90	270.7
Hirano	0.77	280.3
Million	1.08	287.5

Fig. 20—Comparison of the volume diffusion coefficient measured in this study (D_v) with published data.^[6] (Data extracted from the fitted model presented in Fig. 4 for pct Ni = 0.)^[17]



Paper	D_0 (cm^2/s)	Q (kJ/mol)
This work	97.9	191.5
Hanatate	24.1	176.2
Krishtal	40	173.6
Krishtal	50	185.8
Lange	0.77	152.3

Fig. 21—Comparison of the grain boundary diffusion coefficient measured in this study (D_{GB}) with results from the literature.^[17]

of PM nickel steels. Relationship between local nickel content and microstructure was also investigated. Wavelength dispersive X-ray spectrometry (WDS) microprobe analysis using X-ray mapping and line scans was used to characterize local nickel concentrations in parts sintered for 30 minutes at 1223 K, 1323 K and 1423 K (950 °C, 1050 °C, 1150 °C) in an 90 to 10 vol. pct $\text{N}_2\text{-H}_2$ atmosphere. The main findings of this research can be summarized as follows:

1. A new WDS approach linking line scans and X-ray maps to concentration maps was proposed. It allowed us to determine several points:
 1. Under the cooling conditions used, *i.e.* cooling rate of 0.75 K/s (between 1173 K and 723 K

(900 °C and 450 °C) pearlite and bainite are the main constituents of the microstructure when the local concentration of nickel is below 2 wt pct Nickel concentrations in the range of 4 to 6 wt pct favor the formation of martensite. Finally, higher nickel content ($\approx 14 \pm 4$ wt pct) cause the presence of retained austenite.

2. Extracted data from the converted maps allowed us to apply Suzuoka's equation and to determine grain boundary and volume diffusion coefficients of admixed nickel in PM nickel steels. Least square analysis has enabled to determine an Arrhenius type diffusion equation comparable to the literature. The resulting equations are:

1. $D_{GB} = 97.9 \exp(-191.5/RT)$ (cm²/s)
2. $D_V = 4.05 \exp(-300.9/RT)$ (cm²/s)

2. Line scans and X-ray maps showed that:

1. Nickel principally diffuses by surface and grain boundary diffusion mechanisms;
2. Volume diffusion is less significant than surface and grain boundary diffusion and, for conventional sintering conditions *i.e.* 30 minutes at 1394 K (1121 °C), does not allow nickel to homogeneously distribute itself in particles having a diameter larger than 40 μm;
3. It is been observed that prealloyed manganese and molybdenum had diffused into locations where original nickel particles were found. Thus, manganese and molybdenum diffusion into nickel-rich areas probably influences local hardenability and microstructure. Nevertheless, this effect of the presence of manganese and molybdenum still needs to be investigated.

ACKNOWLEDGEMENTS

This work has been carried out with the financial support of the Natural Sciences and Engineering Research Council of Canada (NSERC) and of the Rio Tinto Metal Powders. The authors would like to acknowledge Dr. Benoit Voyzelle for the dilatometry testing.

REFERENCES

1. R.M. German: *Powder Metallurgy and Particulate Materials Processing*, Metal Powder Industries Federation, Princeton, NJ, 2005.
2. J.R. Welty, C.E. Wicks, R.E. Wilson, and G. Rorrer: *Fundamentals of Momentum, Heat, and Mass Transfer, 4 th edn*, John Wiley & Sons, New York, 2001.
3. I Kaur, Y Mishi, and W Gust: *Fundamentals of Grain and Interphase Boundary Diffusion*, 3rd ed., John Wiley & Sons, New York, 1995.
4. MPIF Standard 35: *Materials Standards for PM Structural Part*, Metal Powder Industries Federation Publication, Princeton, NJ, 2009.
5. F. Castro: *Standard Sinter Hardening of PM Steels: A review, Special Interest Program 4: Sinter Hardening and Leaner/Economic Powders; PowderMet 2011*, San Francisco, CA, May 18–21.
6. B. Million, J. Růžičková, J. Velišek, and J. Vřeštál: *Mater. Sci. Eng.*, 1981, vol. 50, pp. 43–52.
7. J. Kučera and K. Stránský: *Mater. Sci. Eng.*, 1982, vol. 52, pp. 1–38.
8. V. Ganesan, V. Seetharaman, and V.S. Raghunathan: *Mater. Lett.*, 1984, vol. 2, pp. 257–62.
9. A. Kohn, J. Levasseur, J. Philibert, and M. Wanin: *Acta Metall.*, 1970, vol. 18, pp. 163–73.
10. J.R. MacEwan, J.U. MacEwan, and L. Yaffe: *Can. J. Chem.*, 1959, vol. 37, pp. 649–54.
11. G.F. Hancock and G.M. Leak: *Met. Sci. J.*, 1967, vol. 1, pp. 33–36.
12. R.M. German: *Sintering Theory and Practice*, John Wiley & Sons, New York, 1996.
13. S.-J.L. Kang: *Sintering, Densification, Grain Growth and Microstructure*, Elsevier Butterworth-Heinemann, London, 2005.
14. S.V. Divinski, F. Hisker, Y.-S. Kang, J.-S. Lee, and C. Herzog: *Interface Sci.*, 2003, vol. 11, pp. 67–80.
15. S.V. Divinski, G. Replitz, and G. Wilde: *Acta Mater.*, 2010, vol. 58, pp. 386–95.
16. R.E. Mistler and R.L. Coble: *J. Appl. Phys.*, 1974, vol. 45, pp. 1507–09.
17. Y. Hanatate: *Mater. Trans., JIM*, 1978, vol. 19, pp. 669–73.
18. J.C. Fisher: *J. Appl. Phys.*, 1950, vol. 22, pp. 74–77.
19. R.T.P. Whipple: *Philos. Mag.*, 1954, vol. 45, pp. 1225–36.
20. T. Suzuoka: *Mater. Trans., JIM*, 1961, vol. 2, pp. 25–32.
21. E. Kreyszig: *Advanced Engineering Mathematics*, 9th ed., John Wiley & Sons, New York, 2006.
22. F. Semel: *Proceedings of PM2TEC2001, International Conference on Powder Metallurgy & Particulate Materials, 2001, New Orleans, Louisiana May 13–17*.